Soft Matter

PAPER

View Article Online
View Journal | View Issue

Cite this: *Soft Matter*, 2025, **21**, 8835

Oxidative destabilization of model *E. coli* membrane by $Cu(OH)_2$ nanoparticles: a neutron reflectometry study

Samantha Micciulla, *[a] Hayden Robertson, [b] Nicoló Paracini †[c] and Gwenaël Corbel *[d]

The rapid rise in antibiotic resistance of several bacterial strains poses a major threat to the efficacy of existing antibiotics. The development of new antimicrobial compounds to treat bacterial infections has indeed become one of the most urgent commitments of this century, both for therapeutics and for purification and decontamination purposes. The use of compounds producing reactive oxygen species (ROS), such as hydroxyl radicals, has been proposed recently as an effective alternative to classical antibacterial agents. Among the suitable compounds, we have focused on the effect of copper hydroxide nanoparticles, $Cu(OH)_2$ (which produce $OH^{\bullet}$ radicals in presence of hydrogen peroxide, H_2O_2) on the structure and stability of a biomimetic membrane of *Escherichia coli*. Our results showed that millimolar concentrations of H_2O_2 were sufficient to prompt the production of ROS from Cu^{2+} and Cu^{+}/Cu^{3+} ions by a Fenton-like redox cycling, which reacted with the lipid unsaturation and broke the symmetric bilayer ordering. By neutron reflectometry we characterized the lipid bilayer structure before and after the exposure to the nanoparticles, and we found that more than 50% of the original bilayer was converted into a single lipid layer, a consequence of its lysis upon peroxidation. This study builds the pillar of a simple but very accurate method to investigate lipid bilayer degradation by bacterial nanoparticles, with the possibility of screening over various membrane composition, nanoparticles chemistry and oxidative media.

Received 6th August 2025,
Accepted 22nd October 2025

DOI: 10.1039/d5sm00809c

rsc.li/soft-matter-journal

1 Introduction

The emergence, evolution and spread of resistance in pathogenic bacteria was declared as a major and serious public health issue by the European Center for Disease prevention and Control (ECDC) and the World Health Organization (WHO)[1] in 2023. In Europe, bacteria resistant to antibiotics cause more than 670 000 infections per year, about 33 000 people die from these infections,[2] with extra healthcare annual costs of around 1.1 billion. In 2022, the French survey on the prevalence of hospital-acquired infections (HAIs)[3] showed that almost half of them were caused by 4 pathogens: the two Gram positive bacteria *Staphylococcus aureus* (12.22%) and *Enterococcus faecalis* (6.99%), and the two Gram-negative bacteria *Escherichia coli* (22.15%) and *Pseudomonas aeruginosa* (6.93%).

The development of new compounds and therapeutic strategies to treat bacterial infections is one of the most urgent commitments and global concerns of this century, while the rapid rise in antibiotic resistance poses a significant threat to the efficacy of existing antibiotics.[4]

Antimicrobial resistance (AMR) occurs when pathogens (bacteria, viruses, fungi or parasites) no longer respond to antimicrobial drugs.[5] As a consequence, infections become difficult or impossible to treat, and the risk of uncontrolled disease spreading, severe illness, disability and death rapidly increases.[6–8] While AMR is a natural process happening over time through genetic changes of all pathogens, the severe misuse and overuse of antibiotics in humans, animals and plants have significantly accelerated this phenomenon. More alarmingly, in 2021 it was estimated that 52.3% of the *E. coli* and 17.2% of *S. aureus* isolates were resistant to the last generation of antibiotics marketed in Europe.[1]

The design of new therapeutic approaches is anything but simple and it relies on an extended knowledge of the mode of action of antimicrobial compounds on bacterial death. Recently,

[a] *Laboratoire Interdisciplinaire de Physique, UMR-5588 CNRS/UGA, 38402 Saint Martin d'Heres, France. E-mail: samantha.micciulla@univ-grenoble-alpes.fr*
[b] *Soft Matter at Interfaces, Institute for Condensed Matter Physics, Technische Universität Darmstadt, 64289 Darmstadt, Germany*
[c] *Institut Laue-Langevin, 38000 Grenoble, France*
[d] *Institut des Molécules et Matériaux du Mans (IMMM), UMR-6283 CNRS/Le Mans Université, 72085 Le Mans Cedex 9, France. E-mail: gwenael.corbel@univ-lemans.fr*
† Current address: European Spallation Source ERIC, Lund, Sweden.

the use of compounds which are able to produce reactive oxygen species (ROS) *in situ* have been proposed for the design of new antimicrobial drugs,[9,10] being lipid peroxidation a critical factor in cell damage.[11] This chemical process occurs when reactive oxygen species, such as hydrogen peroxide, attack and oxidize unsaturated fatty acids in cell membranes. The removal of an electron from a fatty acid molecule generates fatty acid radicals, which react with molecular oxygen to produce peroxyl radicals.[12,13] When such radicals further react with other fatty acid molecules, the lipid peroxidation propagates,[14] forming further reactive lipid peroxides which can finally cause covalent modification of proteins and nucleic acids.[11,15] Since lipids are responsible for maintaining the integrity of cellular membranes, extensive peroxidation of lipids alters the assembly, composition, structure, and dynamics of lipid membranes, which can lead to fatal leakage of cellular components.

Metal nanoparticles have been recently reviewed as very interesting materials with potential antimicrobial activity, including copper-based nanoparticles.[16] Non-soluble cupric oxide (CuO) nanoparticles[17–22] are known for their antibacterial effect on the pathogens responsible for hospital-acquired infections. Recently, we have also shown that 100% reduction of initial inocula of *S. aureus* or *E. coli* (one million CFU per mL (Colony Forming Unit per mL), 6 $\log_{10}$ reduction) occur on contact with $Cu(OH)_2$[23] nanorods after only 3 h at 20 °C, without UV irradiation. This bactericidal performance exceeds that of cupric oxide nanoparticles evaluated under the same conditions.[23] In the presence of H_2O_2, a by-product of cell respiration in aerobically living organisms[24] and present in millimolar concentration in the culture supernatants of *S. aureus* and *E. coli*,[25] cupric ions catalyze the generation of superoxide $O_2^{-\bullet}$ and hydroxyl $OH^\bullet$ radicals through a Fenton-like redox cycling between Cu^{2+} and Cu^+/Cu^{3+} ions.[26] An electron paramagnetic resonance (EPR) study using DMPO (5,5-dimethyl-1-pyrroline N-oxide) as a diamagnetic spin trap molecule revealed that 70% of the radicals produced by $Cu(OH)_2$[23] nanorods in water are $OH^\bullet$ radicals. These hydroxyl radicals are extremely reactive towards organic molecules such as lipids, as they can initiate a free radical chain reaction leading to their peroxidation. Interestingly, the mass concentration of cupric ions released from nanorods measured by atomic emission spectroscopy[23] is several tens of times lower than minimum inhibitory concentrations (MICs) for the growth of *S. aureus* and *E. coli*,[27] which suggests that the antimicrobial activity is not trigger by the ions in solution. Indeed, the $OH^\bullet$ radicals can only be produced by the adsorption and dissociation of hydrogen peroxide molecules on the surface of the nanorods (heterogeneous catalysis). This implies that the antimicrobial effect of $Cu(OH)_2$ nanorods is related to this surface process, and consequently they must be absorbed onto the bacterial outer membrane to release radicals nearby. Although this mechanism is the only one capable of explaining the bactericidal effect of nanorods, no study has yet proved it experimentally. Importantly, the potential use of metallic copper as an alternative to stainless steel in hospitals has been presented in research works, supported by the promising results of its efficacy against nosocomial pathogens.[28,29] Such effect indeed relies on the bactericidal activity of its corrosion products, CuO and $Cu(OH)_2$, growing as thin layer in ambient conditions ($\approx$60% relative humidity and room temperature) within 24 hours.[30]

The cell of common Gram-negative bacteria is surrounded by a double membrane envelope, consisting of an outer and a cytoplasmic membrane, separated by a thin layer of peptidoglycans.[31] The cytoplasmic membrane and the inner leaflet of the outer membrane are mostly composed of phospholipids, whilst the outer leaflet of the outer membrane contains lipopolysaccharides. The major phospholipid components are the zwitterionic 1-palmitoyl-2-oleoyl-*sn-glycero*-3-phosphoethanolamine (POPE), the anionic 1-palmitoyl-2-oleoyl-*sn-glycero*-3-phospho-(1′-rac-glycerol) (POPG) and 1,3-bis(*sn*-3′-phosphatidyl)-*sn*-glycerol (BPG or cardiolipin).[32] In *E. coli*, the POPE : (POPG : BPG) ratio ranges approximately from 75 : 25%$_{mol}$ (cytoplasmic membrane) to 90 : 10%$_{mol}$ (outer membrane), with BPG content of just a few percent for certain strains.[33,34] To perform biophysical studies, model membranes are conveniently reconstituted onto solid substrates in the form of solid supported bilayers (SLBs).[35] SLBs allow preserving the fundamental features of highly complex biomembranes (bilayer thickness, lipid mobility, protein insertion) while being extremely versatile for a wide range of surface-sensitive techniques.[36–39] In addition, the use of supported bilayers is not limited to the study of biologically relevant models, but it can be exploited to create formulation of biotechnological relevance, including for the design of specific liposome formulations for pharmaceutical uses.[40,41] For a continuous coverage of a substrate with a planar bilayer, Langmuir–Blodgett deposition[42] and vesicles fusion[43] are the most widely exploited approaches. Vesicle fusion involves adsorption, spontaneous rupture and spreading of small unilamellar vesicles (<100 nm diameter) onto a solid support, and it has become a standard method for bilayer formation[44–46] thanks to its applicability to a large variety of techniques, sample environments, substrate dimensions and for *in situ* bilayer formation. However, while the method provides high quality bilayers with a rather large variety of lipid mixtures, in particular for mammalian membranes,[46] vesicle fusion can be challenging to master for more complex biomimetic mixtures; specifically, when they contain lipid of conical shape (the case of POPE, for instance),[47] or in case of weak vesicle-substrate interactions, when vesicles tend to preserve their curved assembly and remain deformed but intact on the surface.[48] Other important parameters which can influence the quality of lipid bilayers are the lipid phase, the vesicle size and lamellarity,[49] and also some inherent substrate properties such as its surface nanoroughness, which has a direct impact on the fusion process and on the mechanical stability of the lipid layer.[50] Last but not least, environmental conditions such as ionic strength, osmotic pressure, temperature, and pH influence both bilayer formation and structural properties.[51–53] Optimal conditions for the lipid bilayer formation are in some cases unattainable, and this represents a non-trivial limitation for biophysical studies chasing very specific phenomena in living systems, and attaining to the closest mimicking of a certain cell membrane. To mimic the phospholipid membrane of Gram-negative bacteria, the use of POPE:POPG liposomes to form SLB onto silicon substrate

has been reported.[54] The described protocol requires high temperature (50 °C) and a very accurate control of the interfacial charge balance to prevent the liposomes aggregation, with consequent irreversible deposition of multilayers of unruptured vesicles. All these aspects, from the liposomes properties to the conditions of the surrounding medium, makes the vesicle-to-bilayer transition very difficult to reproduce on different substrates, in particular if they present slightly higher nanoroughness[50] or a large surface area.

As an alternative technique to form SLB, we have employed the solvent assisted lipid bilayer (SALB) method.[55] This approach does not require the preparation of vesicles, therefore it overcomes the limitations related to vesicle propriety and traditional challenges associated to the vesicle fusion, while being compatible with a large variety of material supports and lipid compositions.[48,56] The preparation of a lipid mixture in water-miscible alcohol, typically isopropanol or ethanol, is needed, and when the solvent is gradually exchanged from alcohol to increasing water fractions, the lipid undergo a phase transition in bulk from inverted micelles, to micelles and finally to liposomes.[55] When the ratio of the aqueous buffer to the organic solvent is low, the adsorbed lipid phase is in dynamic equilibrium with the dissolved lipid phase, and while the solvent exchange proceeds, the lipid phase forms a complete supported lipid bilayer.[57]

In this work, we present the preparation of model cytoplasmic membrane of *E. coli* bacteria and its degradation by the reactive oxygen species (ROS) produced by $Cu(OH)_2$ nanorods. To prepare the model membrane, a mixture of POPE : POPG 85 : 15%$_{mol}$ was selected, a valid intermediate composition between inner (75 : 25%$_{mol}$) and outer (90 : 10%$_{mol}$) membranes.[33,54] Supported lipid bilayers were prepared onto silicon substrates by the SALB method. Our results demonstrate (1) the formation of perfectly ordered, densely packed and stable POPE:POPG bilayers over a large surface (80 × 50 mm^2), at room temperature and using Ca^{2+}-free aqueous buffers, and (2) their significant peroxidation upon exposure to $Cu(OH)_2$ nanorods in presence of millimolar concentration of H_2O_2. Preliminary quartz crystal microbalance with dissipation (QCM-D) experiments have served for the protocol optimization and to identify possible variations of the bilayer due to the peroxidation process, in particular the formation of defects and structural heterogeneity. These results have anticipated an accurate structural analysis performed by neutron reflectometry (NR), where contrast variation and nanoparticle matching conditions were exploited to confirm the extent of bilayer degradation and characterize the interfacial structure after the exposure to $Cu(OH)_2$ nanoparticles. More specifically, when the lipid bilayer was exposed to the $Cu(OH)_2/H_2O_2$ medium, more than half of its structure was decomposed to a single lipid layer. Interestingly, control experiments conducted on an equal POPE : POPG bilayer exposed to H_2O_2 medium without $Cu(OH)_2$ nanoparticles have shown that the structure was almost fully preserved, proving the compelling role of the $Cu(OH)_2$ as a catalyst for the dismutation of H_2O_2 into free oxygen radicals.

The results are very promising for the design of disinfection strategies exploiting ROS as agents for the destabilization of bacterial membranes, and its applications spans over various fields, including agriculture, health, material science and biotechnology. The method is not exclusively valid for $Cu(OH)_2$ nanoparticles, but the principle can be extended to other bactericidal nanoparticles which share similar mechanisms and have different surface chemistry.[58]

2 Methods

2.1 Materials

Chloroform (≥99.9%), ethanol (≥99.8%), acetone (≥99.9%), isopropyl alcohol (IPA, ≥99.5%), sodium choride (NaCl, ≥99%) and tris(hydroxymethyl)aminomethane (Tris, ≥99.8%) were purchased by Merck (Germany). Deuterated water (D_2O, isotopic purity 99.9%) was from Eurisotop (France). The lipids 1-hexadecanoyl-2-(9*Z*-octadecenoyl)-*sn-glycero*-3-phosphoethanolamine (POPE, ≥99%) and 1-hexadecanoyl-2-(9*Z*-octadecenoyl)-*sn-glycero*-3-phospho-(1′*rac* glycerol) sodium salt (POPG, ≥99%) were purchased from Avanti Polar Lipids (Alabama, US). Double deionized ultrapure water (18.2 MΩ cm) was obtained from a water purification station (Merck Millipore, Germany). $CuCl_2{\cdot}2H_2O$ (99%, AppliChem Panreac, Germany), H_2O_2 (30–32% w/w in H_2O, Fisher Chemical, UK), NaOH (97% pellets (Supelco Emplura, Merck, Germany) and Na_2CO_3 (≥99.5%, Merck, Germany) were used as received.

2.2 Nanoparticles preparation

Nanoparticles of $Cu(OH)_2$ were successfully prepared at room temperature by precipitation in a mixed alkaline (NaOH/Na_2CO_3) medium. Briefly, 50 mL of a 0.5 M cupric chloride dihydrate solution was added dropwise to 150 mL of a freshly prepared mixture of 0.6 M NaOH and 0.1 M Na_2CO_3 solutions under stirring. After complete delivery of the cupric chloride solution, the suspension was stirred for 3 h and then aged for 15 h without stirring. A full decantation by gravity of the blue nanorods took place during this aging period. After decantation, it is necessary to remove sodium salts (carbonate and chloride) from the resulting precipitate. The precipitate is then washed with hot deionized water and centrifuged five times at 4000 rpm for 5 min by using a Sigma 3–16 L centrifuge. After the last washing with hot water, the suspension of nanorods is drawn through a Büchner funnel by vacuum suction to recover them on a filter paper. The filter paper with nanorods is left to dry overnight in a fume hood. The nanoparticles are rod-shape with dimension of about 15 nm × 200 nm (nanorods), the ζ-potential measured in MilliQ water (pH = 5.5) was +22.9 (± 0.2) mV.

Although this is a very slow process occurring over several hours, a progressive H/D exchange can occur over time as the $Cu(OH)_2$ nanorods are immersed in D_2O. To ensure the isotopic stability for neutron reflectometry experiments when the sample is injected onto the SLB, the suspension was prepared at least 48 hours in advance. $Cu(OH)_2$ has two non-equivalent hydroxide ions within its crystal structure,[23] thus explaining the presence of two distinct stretching vibration ν_{OH} bands in its IR spectrum (Fig. S3). As in other metal hydroxides,[59] the partial exchange of the proton by the deuteron leads to the appearance

of vibrational stretching ν bands of the O–D bond shifted to low wavenumbers of about 100 cm^{-1} compared with those of the O–H bond, whose vibrational band decreases in intensity at the same time. The exchange rate estimated by calculating the integrated intensity ratio of the bands is approximately 25%, which gives the following formulation $Cu(OH)_{1.5}(OD)_{0.5}$. The SLD of this mixed hydrogenated:deuterated copper hydroxide is equal to 3.5×10^{-6} $Å^{-2}$,[60] and this SLD was used as reference for the preparation of nanoparticle matching water, NPMW. By matching the signal produced by the nanoparticle layers, the reflectivity curve results from neutrons reflected by the lipid layer only, which simplifies significantly the analyses of the variation of the lipid layer as consequence of the lipid peroxidation.

2.3 Solid supported lipid bilayer (SLB) preparation

Stock solutions (2 mg mL^{-1}) of each lipid, POPE or POPG, were prepared in isopropyl alcohol (IPA). Aliquots of each lipid solution were mixed to obtain POPE : POPG 85 : 15%$_{mol}$ mixtures at final concentration of 0.5 mg mL^{-1}. Solid supported bilayer (SLB) were prepared by SALB method[55] onto either SiO_2-coated quartz crystal (QSX-303 from Biolin Scientific, Sweden, roughness $\leq$10 Å) or Si single crystal (single-side polished, $\langle 111 \rangle$, 80 × 50 × 15 mm^3). Both substrates were cleaned by sequential immersion in chloroform, ethanol, acetone and water (20 min in each solvent) under sonication, followed by UV-Ozone irradiation (ProCleaner Plus, BioForce Nanoscience, Germany) for 30 min prior to use. The silicon substrates for NR experiments were characterized in D_2O to prove the substrate quality prior to lipid deposition. For the SLB formation, a sealed chamber containing the substrate was pre-filled with IPA at 20 °C. The lipid mixture was injected into the cell at a flow rate of 0.1 mL min^{-1}, and let incubate for 20 min. Afterwards, the solution was slowly replaced by an aqueous Tris–NaCl buffer solution (10 mM Tris, 100 mM NaCl, pH = 7.4) prepared in Milli-Q water, which gradually promoted the transition of lipids from free molecules, to inverse micelles and finally liposomes, which fuse onto the solid substrate forming a flat bilayer.[48] The so-formed bilayers were used for the peroxidation studies. Their structural quality was proven both by QCM-D and NR data.

2.4 Quartz crystal microbalance with dissipation monitoring (QCM-D)

QCM-D measurements were carried out on a QSense Analyzer to validate the bilayer formation and run preliminary peroxidation studies. A SiO_2-coated quartz crystals was cleaned according to the protocol described above, then sealed in a QCM-D flow chamber. The cell was filled with the Tris–NaCl buffer at 20 °C, the quartz crystal was calibrated to its resonant frequency and higher overtones. The frequency shift (Δf) and dissipation change (ΔD) were monitored until they reached a stable value. This reference value was set to ''zero'' and the data acquisition was started. After 10 min, the aqueous buffer in the chamber was replaced by IPA (10 min), followed by the lipid mixture (POPE : POPG 85 : 15%$_{mol}$, 0.5 mg mL^{-1} in IPA). Lipids were incubated for 10 min, then the organic solvent was slowly replaced by the Tris–NaCl buffer, which promoted the formation of a supported bilayer onto the substrate. To study the bilayer degradation, a suspension of $Cu(OH)_2$ nanorods in 0.1 mM H_2O_2 solution in MilliQ water was prepared just before use. The Tris–NaCl buffer in the QCM-D flow cell was first replaced by 0.1 mM H_2O_2 solution, followed by the $Cu(OH)_2$ suspension (1.0 mg mL^{-1}) in the same solvent (0.1 mM H_2O_2 in MilliQ water). The nanoparticle suspension was injected for 15 min with a flow rate of 0.1 mL min^{-1}, then the flow was stopped and they were let incubate for 3 hours (static mode). After this time, the Tris–NaCl buffer was flowed in the chamber to remove the nanoparticle layer. Finally, 1 M HCl solution was used to clean flow chamber and tubings and to solubilize any nanoparticles residual. The temperature was kept constant at 20 °C for the entire experiment. Δf and ΔD values were registered for all overtones (from 1st to 13th overtone), the signals from 5th to 11th were selected for the data interpretation and reported in the Results section of this manuscript. The experiment was carried out at 20 °C, all injections and rinsing steps were performed at the same flow rate of 0.1 mL min^{-1}.

2.5 Neutron reflectometry

2.5.1 Data acquisition. Neutron Reflectometry (NR) experiments[61] were performed on the time-of-flight (TOF) neutron reflectometer FIGARO[62] at the Institut Laue-Langevin (ILL, Grenoble, France). Single crystal $\langle 111 \rangle$ silicon blocks were cleaned as described above and sealed in the solid/liquid cells provided by the ILL. Each cell was filled with D_2O for alignment and pre-characterization of the native SiO_2 layer. The beam portion reflected at the same angle (specular reflectivity) was accounted for the analysis, and the ratio between reflected and incident intensity, $R = I/I_0$, was recorded as a function of the momentum transfer $q_z = |k_f - k_i| = (4\pi/\lambda)\sin\theta$, the scattering vector component perpendicular to the interface. Since this is the sole component reported in the manuscript, we will refer to that as q in the rest of the text. The experiments were performed at two incident angles, $\theta = 0.7°$ and 3.0°, using a wavelength spectrum of $2 \leq \lambda \leq 20$ Å, corresponding to a q-range between 0.008 and 0.3 $Å^{-1}$, with $\delta q/q$ = 7%. To avoid ambiguities in the model reproducing the experimental reflectivity data, the systems were measured in three different isotopic contrast varying the SLD of the bulk solution. For this purpose, Tris–NaCl buffer was prepared in D_2O ($\rho_{D_2O} = 6.35 \times 10^{-6}$ $Å^{-2}$), H_2O ($\rho_{H_2O} = -0.56 \times 10^{-6}$ $Å^{-2}$), and a H_2O : D_2O mixture (40 : 60 v/v) to match the $Cu(OH)_2$ nanoparticle SLD (NPMW = 3.5×10^{-6} $Å^{-2}$). The matching conditions NPMW was a convenient contrast to monitor the structural variation of the lipid bilayer during exposure to the nanoparticle solution and eliminate the scattering from the nanoparticle layer, ultimately highlighting the nanostructure of the lipid bilayer.

These experimental settings are recalled later in the text as NR (1). A different instrumental configuration was used to monitor the variation of reflectivity by fast acquisitions (5 min) in the mid-q range and NPMW contrast during the exposure of the bilayer to the nanoparticles, and it is designated as NR (2). Finally, full q-range measurements in NPMW only after the total exposition

time (90 min) are specified as NR (3). More details for each experimental condition are given along with the corresponding results in the next sections.

All SLD values were calculated from the NIST website[60] and using 0.997 g mL^{-1} and 1.105 g mL^{-1} for the density of H_2O and D_2O, respectively.

2.5.2 Data analysis. Neutron reflectivity datasets were analyzed using the *refnx* Python package.[63] An example of the script used to fit the reflectivity data is reported in the SI and is available from the Zenodo repository.[64] In our model, the structure probed by the neutron beam is defined by a sequence of slabs, namely silicon (Si), silicon oxide (SiO_2), proximal lipid headgroups (LH), lipid tails (LT), and distal lipid headgroups (LH), from fronting to backing. Water (W) is accounted in each layer as solvent fraction for all isotopic contrasts. The LH slab is duplicated on either side of the LT slab. Since the two lipid headgroups (LH) layers are identical in nature, they are described by the same parameters in our model. Each layer is defined by four parameters: thickness, scattering length density (SLD), roughness and volume fraction (ϕ). The SLD is the value which describes the interaction of each atom nucleus with the neutron radiation, and it is defined as the sum of the scattering lengths (b) divided by the unit volume for all components in the system,

$$\mathrm{SLD} = \sum_i \rho_i = \frac{N_A \rho}{m} \sum_i b_i \quad (1)$$

where ρ is the density, m the relative formula mass and N_A the Avogadro constant.

To describe our system before and after the exposure to the $Cu(OH)_2$ nanoparticles, two models were employed. The first model (Model 1) describes a pristine POPE:POPG bilayer, and the second model (Model 2) is the combination of the pristine POPE:POPG bilayer and a single lipid layer, labeled "Degraded Lipid Layer" (DLL). The DLL is formed by lipid molecules reacting with the ROS, resulting in a loss of the double-leaflet assembly due to the peroxidation of the alkyl chains.[65] In both models, the position $z = 0$ denotes the start of the SiO_2 layer, so that all the layers following the Si substrates occupy the $z > 0$ range. The silicon substrate is a semi-infinite continuum with $\rho_{Si} = 2.07 \times 10^{-6}$ Å^{-2}.[60] The SiO_2, LH and LT are homogeneous slabs with constant SLD, while thickness, roughness and solvent fraction of each layer are allowed to vary. The SLD values are set to $\rho_{SiO_2} = 3.47 \times 10^{-6}$ Å^{-2}; $\rho_{LH} = 2.5 \times 10^{-6}$ Å^{-2};[54] $\rho_{LT} = -0.30 \times 10^{-6}$ Å^{-2}.[54]

Model 2 fits the datasets for the SLB after exposure to $Cu(OH)_2$ nanoparticles, and it accounts for the relative contribution to the total reflectivity of each system, the residual pristine bilayer and the DLL, by a scale factor. This factor is allowed to vary during the fit, together with the bilayer water fraction, and with the thickness, SLD and roughness of the DLL. The other structural parameters of the pristine bilayer are kept constant. Data from the three different contrasts were co-refined to increase statistical confidence. All SLD and ϕ profiles were extracted from the median model from the Markov Chain Monte Carlo (MCMC) sampling chain. The best fitting model parameters are summarized in Tables S1 and S2 of the SI. For the detailed description of the adopted model we address the reader to the Jupyter notebook (available from ref. 64 and in the SI).

We highlight that models employing the incoherent summation of the reflectivity from the residual bilayer and a bare SiO_2 surface were also examined, to verify the hypothesis of a naked substrate left behind the bilayer rupture. However, this model yielded a poor fit to the experimental data, and the additional lipid layer was therefore necessary to describe the experimental data. These results are available in the SI.

3 Results and discussion

3.1 Bilayer formation and preliminary peroxidation studies by QCM-D

Fig. 1(A) shows the results of a QCM-D experiment aimed at studying the POPE:POPG SLB formation onto Si/SiO_2 substrate at 20 °C. The reported parameters are the frequency shift Δf, which is proportional to the mass per unit area adsorbed onto the surface, and the change of dissipation ΔD, which is a measure of the energy dissipated by the system following the oscillation of the underneath substrate, and therefore related to the film viscoelasticity.[66] The measurement was started when the flow chamber was filled with Tris–NaCl, and multiple overtones were recorded simultaneously. To prepare the SLB, the aqueous buffer was replaced by the organic solvent, IPA, which produced a large variation of Δf and ΔD, including overtones splitting, due to the change of solvent density compared to the aqueous medium. After equilibration, the lipid solution was injected and a small decrease of Δf was measured, similar to previous similar cases[57] and explained by the formation of lipid monolayer islands onto the substrate, in dynamic equilibrium with the bulk lipids.[48] The lipid solution was incubated for 10 min, followed by the injection of Tris–NaCl to gradually promote the transition from bulk aggregates to a supported bilayer. In fact, the experimental values of $\Delta f = -22$ Hz and $\Delta D = 1.6 \times 10^{-6}$, and the merging of all overtones on a single trace, are typical of a flat bilayer, with a relatively high surface coverage and low percentage of defects.[67] Interestingly, the QCM-D data reported in Fig. 1 align with previously reported data for mixed bilayer of zwitterionic and positively charged lipids.[40]

The reproducibility of this sample preparation was confirmed by three repeated QCM-D experiments with a degree of variability ±0.60 Hz for Δf and ±0.5 (10^{-6}) for ΔD. A much larger variability of the results and a lower bilayer quality was obtained when performing the same experiments employing vesicle fusion.[54] Therefore the SALB method was the preferred methodology to prepare SLB for all our experiments with this specific lipidic formulation. For comparison, we have included in the SI examples of QCM-D experiments for SLB preparation applying these two methods (Section 1.1 of the SI).

In the same experiment, the effect of $Cu(OH)_2$ nanoparticles on the properties of the POPE:POPG bilayer was also studied. Fig. 1B reports Δf and ΔD data upon injection of 1 mg mL^{-1}

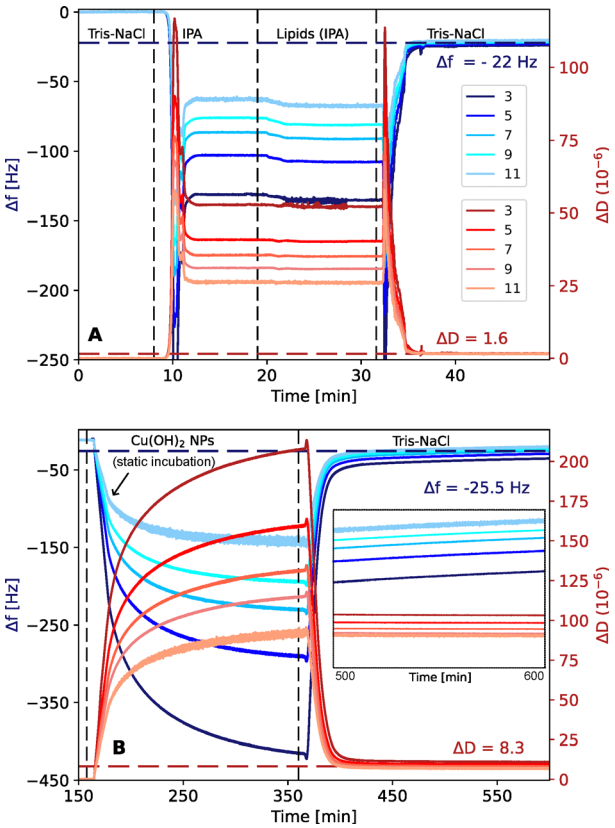

Fig. 1 Frequency shift (Δf) and dissipation energy (ΔD) measured during the preparation of POPE:POPG lipid bilayer by the SALB method (A), followed by the injection of $Cu(OH)_2$ nanoparticles in presence of 0.1 mM H_2O_2 (B). Bilayer preparation, (A) the QCM-D flow cell is pre-filled with Tris–NaCl buffer solution, replaced by isopropyl alcohol (IPA), and then by a solution of (POPE : POPG, 85 : 15%$_{mol}$) lipids in IPA. After 10 min of incubation, the system is rinsed by Tris–NaCl to promote the formation of the supported bilayer, as explained in the Experimental section. The final frequency shift (−22 Hz) and dissipation (1.6×10^{-6}) are within the typical values of a supported bilayer adsorbed onto SiO_2-modified QCM-D substrate. $Cu(OH)_2$ nanoparticles injection, (B) the flow chamber is pre-filled with 0.1 mM H_2O_2 solution in H_2O, followed by the injection of 1.0 mg mL^{-1} $Cu(OH)_2$/0.1 mM H_2O_2 solution. The nanoparticles are incubated for 3 h, the arrow indicates the beginning of the incubation in static mode. This is followed by a final rinse with Tris–NaCl. The inset of this figure reports the Δf and ΔD traces at the end of the preparation, to highlight the final overtone splitting. The QCM-D data of the complete experiment are reported in Fig. S1 of the SI.

$Cu(OH)_2$ solution in 0.1 mM H_2O_2 (10 min), followed by a long incubation (3 hours) and final rinsing with Tris–NaCl buffer. Importantly, just before the nanoparticle injection the chamber was filled with 0.1 mM H_2O_2 solution in MilliQ water, a typical peroxide concentration produced by the normal metabolism of oxygen in bacterial cells[68] and also the typical peroxide concentration found in the culture supernatants of *S. aureus* and *E. coli*.[25] Furthermore, this peroxide concentration is lower than the minimum concentration of 1 mM inhibiting the growth of *E. coli*.[69] The H_2O_2 injection produced minor variation of the QCM-D signal, $\Delta(\Delta f) \approx +8$ Hz and $\Delta(\Delta D) \approx -0.8 \times 10^{-6}$ without overtone splitting, due to change of the properties of the medium (Fig. S1 in the SI). This baseline was the reference for the deposition of the nanoparticles, as shown in Fig. 1B. The injection of the nanoparticles onto the SLB (15 min, 0.1 mL min^{-1}) produced a steep Δf decrease, followed by a slower kinetics during their incubation without solution flow (static mode), as indicated by the black arrow in Fig. 1.

The large overtone splitting is a typical sign of a frequency-dependent behavior (viscoelastic character), and it can be an indication of a major structural heterogeneity in the direction of the acoustic wave propagation (perpendicular to the substrate). In our case, this can be explained by the deposition of the nanoparticles onto the SLB, forming a thick and highly hydrated layer. After rinsing, Δf went back to a similar value than that measured for the lipid bilayer alone, $\Delta f = -25.5$ Hz, which indicates the successful removal of the nanorods. However, the final ΔD was about 5 times larger than the initial value, $\Delta D = 8.3 \times 10^{-6}$, which suggests a more loosely structure than a compact bilayer, a possible consequence of a partial lipid peroxidation in our SLB. The formation of defects in the bilayer can well explain the overtone splitting, as highlighted by the inset in Fig. 1B. The presence of residual nanoparticles is a more unlikely scenario compared to the formation of cavities in the lipid structure filled by aqueous solution. Our hypothesis is reasoned by two main aspects: first of all, in presence of residual nanoparticles, given the large size of the nanorods one would expect a larger shift in both frequency and dissipation; secondly, the formation of coordination complexes between cupric ions, Cu^{2+}, and Tris buffer at standard physiological conditions (NaCl, pH = 7.4) significantly weakens the electrostatic interactions with the lipid bilayer.[70] Accordingly, the rinsing step with Tris–NaCl should already be sufficient to remove most nanoparticles. In addition, the low solubility product constant ($K_{SP} = 2.2 \times 10^{-20}$) of $Cu(OH)_2$ results in a very low concentration of free cupric ions, which is of the order of 11 μg L^{-1}, therefore we expect most nanoparticles preserving their 2D-dimensional structure of periodic stacking of staircase-shaped $[Cu(OH)_2]_\infty$ layers along the crystallographic b direction. Nevertheless, since trace amounts cannot be completely ruled out from the QCM-D data, in the NR experiments an additional rinsing step with 1 M HCl was included, which ensures the complete nanoparticle solubilization before the final bilayer characterization.

For the sake of completeness, the full QCM-D experiment, including the change of surrounding solution from buffer to H_2O_2 solution, is reported in Fig. S1 of the SI. A typical scatter plot ΔD *versus* Δf, which directly correlates the variation of sensed mass (adsorption) to the change of energy dissipation (viscoelastic behavior), is also included in Fig. S4 of the SI. In particular, this analysis helps to distinguish between the variations related to the change of solvent properties and those related to the surface phenomena, such as the bilayer formation, the nanoparticles sedimentation and their removal. Lastly, the decrease of $-\Delta f$ at constant ΔD after the final rinse with Tris–NaCl buffer suggests the loss of some material from the bilayer, since the sensed mass decreases while the viscoelastic properties of the film remain unchanged.

3.2 Impact of peroxide concentration on the bilayer structure

The preliminary QCM-D study has delivered important information on the bilayer quality, on the feasibility of the peroxidation experiments and on the variation of the bilayer density produced by the lipid peroxidation. However, it did not provide accurate information on the internal bilayer structure and on the residual lipid : water ratio in the film. Neutron reflectometry (NR) experiments provided complementary information to clarify the volume fraction distribution of the lipids at the interface, and to help identifying the variation associated to their peroxidation upon the direct comparison of the reflectivity data before and after the process.

For the NR experiments on the first POPE:POPG bilayer, we have adopted the schematic sequence reported in Fig. 2. Briefly, the structure of the lipid bilayer was characterized directly after sample preparation in three isotopic contrasts (D_2O, NPMW, H_2O), then the nanoparticle suspension, 1.0 mg mL^{-1} $Cu(OH)_2$ nanoparticles in presence of 0.1 mM H_2O_2, was injected in the solid/liquid cell and let equilibrate for 90 min. During the incubation, short reflectivity acquisition were performed (5 min) for a total time of 90 min. The H_2O_2 concentration was sequentially increased to 0.3 mM and 30 mM to boost the peroxidation process. A peroxide concentration of 0.3 mM remains below the minimum inhibitory concentration (MIC) of 1 mM for *E. coli*,[69] whereas a concentration of H_2O_2 equal to 30 mM is much higher. Actually, this concentration was reported by Imlay *et al.*[71,72] who have shown that *E. coli* can survive doses of up to 30 mM H_2O_2 if it has been previously exposed to doses below the MIC, which is the scenario of our experiment. Finally, the sample was rinsed with 1 M HCl solution to ensure the complete removal of any nanoparticle traces. The structure of the lipid bilayer, after peroxidation and complete nanoparticle solubilization, was characterized again over the full q-range and with isotopic contrast variation.

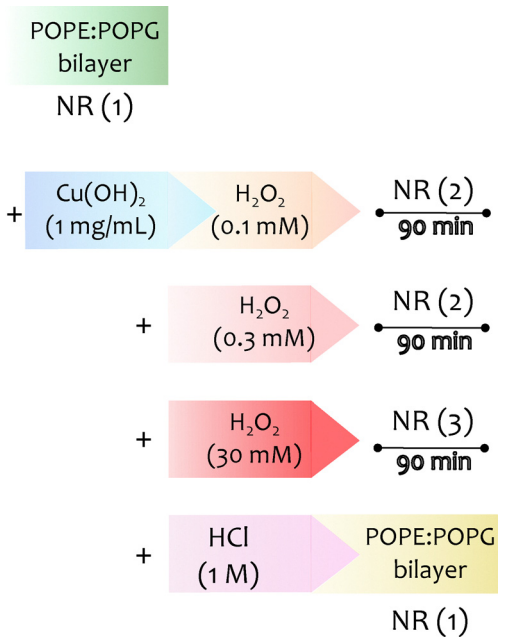

Fig. 2 Schematic representation of the sequence of the sample preparation and NR measurements performed on the first POPE:POPG lipid bilayer. The label NR (1) indicates the NR structural characterization of the lipid bilayer on the full q-range and with three isotopic contrasts (D_2O, NPMW and H_2O), in absence of nanoparticles; NR (2) indicates the NR kinetics at intermediate q-range and short data acquisition to monitor the evolution of reflectivity during the exposure of the bilayer to the $Cu(OH)_2$/H_2O_2 environment; NR (3) corresponds to a full q-range measurement during exposure of the bilayer to the $Cu(OH)_2$/H_2O_2 suspension in NPMW contrast only.

To prepare the lipid bilayer at the FIGARO beamline, a POPE:POPG solution (0.5 mg mL^{-1}) in IPA was injected in three solid/liquid cells containing a silicon substrate. As described above, measurements of the SLB were taken in three isotopic contrasts (D_2O, NPMW and H_2O) before (initial state) and after (final state) exposure to the $Cu(OH)_2$ nanoparticles. Importantly, the characterization of the sample in its final state was performed after complete removal of the nanoparticles by HCl rinsing. The purpose of this approach was to mask the reflectivity from the nanoparticles layer and highlight only the structural variation of the lipid bilayer. Fig. 3 reports the reflectivity data, SLD and best fitting volume fraction profiles of the pristine POPE:POPG bilayer (panels A–C) and the post-peroxidation bilayer (panels D–F); the corresponding best fitting model parameters are reported in Table S1 of the SI. First of all, the results for the pristine bilayer demonstrated the formation of a high-quality SLB, with high lipid packing density (<2% water in lipid tails, LT, Fig. 3C). The successful formation of a SLB of this lipidic composition and complete coverage over such a large substrate (80 × 50 mm^2) represents a crucial achievement of this work. As mentioned in the introduction, a previous experimental work has reported the preparation of a similar SLB onto quartz/SiO_2 and silicon substrate by vesicle fusion, but the applied protocol required high temperature, a continuous flow of the lipid solution, and a highly accurate control of Ca^{2+} concentration and osmotic pressure.[54] The required experimental conditions for the success of the reported protocol have been very challenging to reproduce in our preliminary experiments, in contrast to the ease handling of the SALB method, which delivered excellent bilayer samples.

To understand the variation of the bilayer structure during the peroxidation process, we compared the structure of the initial bilayer with the structure of the same sample after exposure to $Cu(OH)_2$. As we expected a heterogeneous structure across the illuminated area of the neutron beam as a result of the possible bilayer degradation, we included in our model the incoherent summation of two reflectivities, one describing the areas where the lipid bilayer maintained its original double-sheet assembly, and the other describing the areas where the degradation led to the formation of a layer of lipids loosing the ordered bilayer arrangement (degraded lipid layer = DLL). This is the Model 2. in the Experimental section. The best fitting model of this post-peroxidation scenario is reported in terms of volume fraction profile distribution in Fig. 3F, along with the best fitting parameters listed in Table S1. The final reflectivity has a contribution of about 15% from the pristine bilayer, and

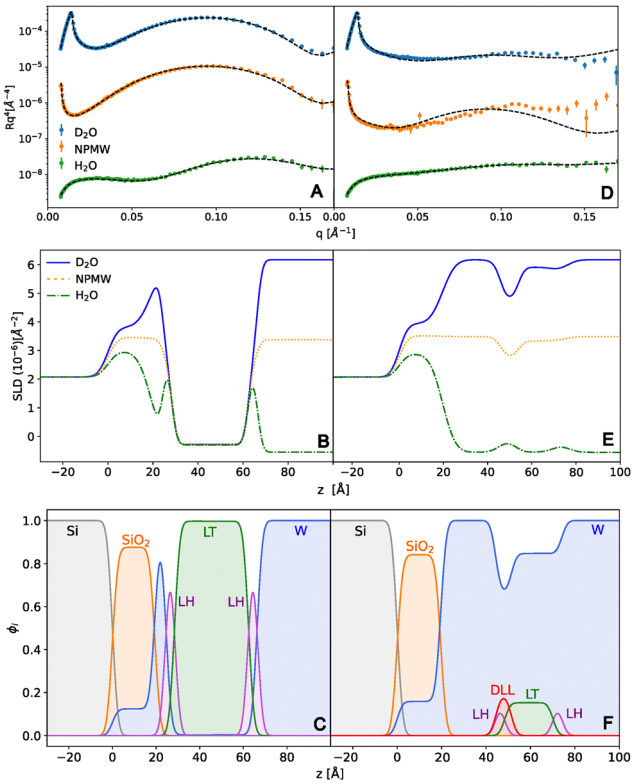

Fig. 3 (A) and (D) Neutron reflectometry data, (B) and (E) SLD profile and (C) and (F) best-matching volume fraction profile (ϕ_i) of POPE:POPG bilayer obtained from the reflectivity fits and according to the solid lines superimposed to the raw data in Panel A and D. Panels A–C are for the pristine bilayer, panels D–F are for the system after peroxidation. For this experiment, $Cu(OH)_2$ nanorods were incubated in presence of increasing H_2O_2 concentration (0.1 mM, 0.3 mM, 30 mM), followed by rinsing with 1 M HCl solution for nanoparticles removal. Labels: silicon substrate "Si", silicon oxide "SiO_2", water "W", lipid heads "LH", lipid tails "LT", degraded lipid layer "DLL".

about 85% of the DLL (partial volume fractions in Fig. S4 of the SI). Each contribution is quantified by the corresponding scaling factor of each reflectivity. The regions of the surface occupied by the DLL are highly hydrated, and the DLL dry mass occupies only about 20% of the total volume, with a thickness of ≈ 8 Å and SLD close to zero. A large water layer between substrate and lipids is formed (from 5 to 33 $\pm$ 2 Å), evidence of the formation of defects in the original bilayer structure and possibly the source of increasing ΔD in our preliminary QCM-D data.

This scenario of a heterogeneous lipidic structure (SLB/DLL) was compared to the case of a SLB/SiO_2 structure. In this model, we construct the incoherent summation of the reflectivities from the pristine bilayer and a bare Si/SiO_2 surface. This represents the case where the degraded lipids loose their assembly and are completely removed from the surface, leaving areas of bare silicon substrate exposed to water. Noteworthy, this model does not change the description of the layer hydration, which is the solvent fraction present in each slab. The increased permeability of a lipid bilayer due to lipid peroxidation is a reported effect in literature,[65] and now our results add molecular details, for this specific system and peroxidation method, of the degraded bilayer. The results of the data analysis assuming the incoherent summation for the SLB/SiO_2 system are reported in Fig. S5 of the SI, where they are compared with the NR data for the SLB before exposure to the $Cu(OH)_2$ nanoparticles (the same as reported in Fig. 3(A)–(C)). The partial volume fraction profile of each system, the SLB and the bare SiO_2 substrate, are shown in Fig. S6. The results allowed us to conclude that the SLB:DLL scenario more suitably described the system structure after exposure to $Cu(OH)_2$ in the oxidative environment.

Several studies on lipid/nanoparticles interaction have reported depth-resolved structural information.[40,41] In our case, this information is not easily accessible from our NR experiments, where the large size of the $Cu(OH)_2$ nanoparticles is likely to produce a strong diffuse scattering, which would interfere with the specular reflectivity. The positive surface charge of $Cu(OH)_2$ nanorods in MilliQ water and the negative of POPE:POPG lipid bilayers leads to an electrostatic attraction between the nanoobjects and the model membrane. In the absence of buffer, the formation of coordination complexes with cupric ions is negligible, and this creates a favorable scenario for electrostatics. In addition, the 2-dimensional structure of cupric hydroxide built up from the periodic stacking of staircase-shaped $[Cu(OH)_2]_\infty$ layers is slightly deficient in hydroxide anion, as evidenced by the positive value of the ζ potential. This condition promotes the coordination of cupric ions on nanoparticle surface with anionic PG groups. Lastly, the large size of $Cu(OH)_2$ nanoparticles induces the sedimentation, driven by gravity, over time, as visible in Fig. 1B. The accumulation of the nanoparticles onto the lipid bilayer surface allows them to produce the ROS in proximity of the lipid layer, and consequently their peroxidation. Surface imaging techniques could add additional information on the arrangement of $Cu(OH)_2$ nanorods onto the lipid bilayer.

3.2.1 Kinetics of bilayer degradation. Intermediate characterization of the SLB during the $Cu(OH)_2$ incubation was carried out only in NPMW using fast kinetic acquisition (5 min) at intermediate q range (0.08 and 0.2 $Å^{-1}$) for total incubation time of 90 min. The specific instrument configuration for the kinetics was selected to focus on the q-region where the increase of LT solvation, a consequence of the bilayer degradation due to lipid peroxidation, is expected to produce a variation of the reflectivity profile. The results are shown in Fig. S7(A)–(C) of the SI for increasing H_2O_2 concentration, 0.1 mM and 0.3 mM, while Fig. S7C reports the variation of reflectivity over time interpolated at $q = 0.05$ $Å^{-1}$, an arbitrary value but within a very sensitive range to the variation of LT hydration. The color gradient from darker to lighter in Fig. S7A and B corresponds to increasing time. As it can be seen from the decrease of Rq^4 in presence of 0.1 mM H_2O_2 (blue data points), there is a small initial decrease of reflectivity, and for $t > 40$ min the data reach a stable value.

To boost the peroxidation process, a more concentrated peroxide solution (0.3 mM) was injected inside the NR cell, which further promote the formation of ROS. The new kinetics acquisition, reported in Fig. S7B and C (green data points) demonstrate a similar decrease initial decrease of reflectivity, sign of the effective boosting of the lipid peroxidation, and the stabilization of the signal at $t > 50$ min.

Finally, the H_2O_2 concentration was further increased to 30 mM, as used in a previous study where the production of free oxygen radicals by $Cu(OH)_2$ nanoparticles was monitored by EPR spin trapping experiments.[2,3] The sample was left under this peroxidative environment for additional 90 min, but without kinetic acquisition for time constraints, finally rinsed with HCl 1 M to remove the nanoparticles. After this treatment, the reflectivity of the sample was measured in the three selected isotopic contrasts, the data are shown in Fig. 3(D)–(F). To highlight the effect of the highest oxygen peroxide concentration (30 mM) on the bilayer integrity, we directly compared the NPMW reflectivities measured at all H_2O_2 concentrations, which are reported in Fig. S8 of the SI. Note that the reflectivities at low-H_2O_2 concentrations (0.1 mM and 0.3 mM) were only measured in the kinetics configuration (within a limited q-range), while the reflectivity of the pristine SLB and after incubation with $Cu(OH)_2$/(30 mM) H_2O_2 were measured within the full q-range. The reader is addressed to the schematic representation of the experiment in Fig. 2 for clarity. A gradual decrease of the total reflected intensity for the two low peroxide concentrations can be observed, in contrast to the abrupt change of the reflectivity for the incubation with $Cu(OH)_2$/(30 mM) H_2O_2 suspension. This result confirms that the peroxide concentration had a strong influence on the rate of lipid peroxidation, most likely by increasing the production of ROS reacting with the unsaturation of the LT.

3.3 Impact of concentrated peroxide solution on the bilayer structure

The NR experiments described above have served as a reference to set the experimental conditions for studying the lipid peroxidation within the available times at the FIGARO beamline. A second experiment was carried out by exposing a POPE:POG bilayer to $Cu(OH)_2$ nanorods suspended in 30 mM H_2O_2 solution, as schematically represented in Fig. 4. According to our previous observation (Fig. S8), this is the most efficient condition for the bilayer degradation.

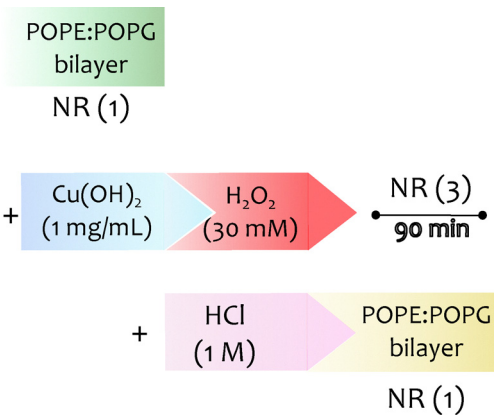

Fig. 4 Schematic representation of the sequence of the sample preparation and NR measurements performed on the second POPE:POPG lipid bilayer. The label NR (1) indicates the NR structural characterization of the lipid bilayer on the full q-range and with three isotopic contrasts (D_2O, NPMW and H_2O); NR (3) corresponds to a full q-range measurement during exposure of the bilayer to the $Cu(OH)_2/H_2O_2$ suspension in NPMW contrast only.

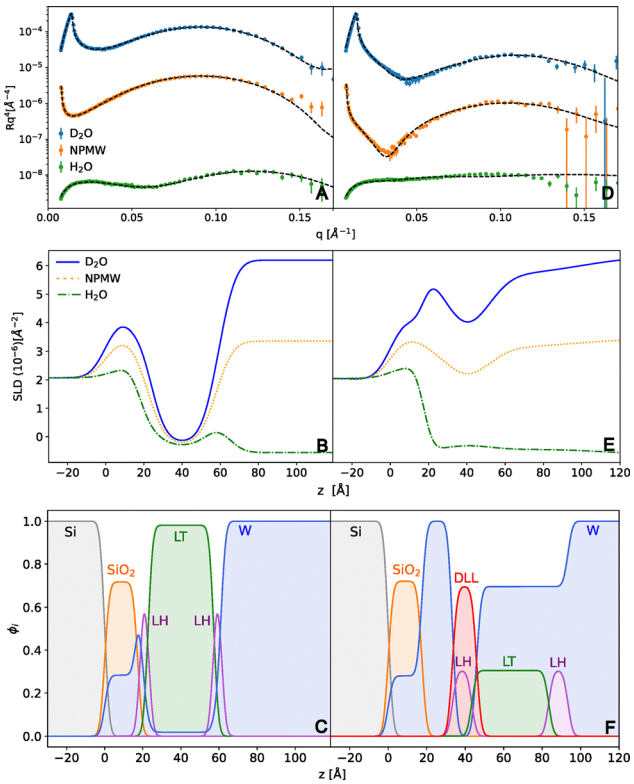

Fig. 5 (A) and (D) Neutron reflectometry data, (B) and (E) SLD profile and (C) and (F) best-matching volume fraction profile (ϕ_i) of POPE:POPG bilayer obtained from the reflectivity fits and according to the solid lines superimposed to the raw data in Panel A and D. Panels A–C are for the pristine bilayer, panels D–F are for the system after peroxidation. For this experiment, $Cu(OH)_2$ nanorods were incubated in presence of 30 mM H_2O_2 for 90 min, followed by rinsing with 1 M HCl solution for nanoparticle removal. Labels: silicon substrate "Si", silicon oxide "SiO_2", water "W", lipid heads "LH", lipid tails "LT", degraded lipid layer "DLL".

Fig. 5 shows the full bilayer characterization of this second sample before (panels A–C) and after (panels D–F) the exposure to $Cu(OH)_2$/(30 mM) H_2O_2 environment and complete removal by HCl rinsing. The reflectivity data were analyzed using the same model as for the first sample, namely a pristine bilayer for the initial state (Model 1), and the incoherent summation of the reflectivities of a bilayer and a single lipid layer for the final state after peroxidation (SLB/DLL, Model 2).

Also in this case, the volume fraction profile ϕ_i for the POPE:POPG bilayer (Fig. 5C) proves the formation of a highly ordered structure with a very high substrate coverage (water fraction $<2\%$ in the LT region). This important outcome of our experiments is the demonstration of the high reproducibility of the SALB method for this biomimetic bacterial membranes. The structural parameters for the best fitting model of this system (thickness, roughness, hydration percentage) are reported in Table S2 of the SI.

After incubation with $Cu(OH)_2$ and rinsing with HCl solution (Fig. 5(D)–(F)), the system was constituted by 30% of the original bilayer, with higher external roughness and thicker LH and LT

regions, and 70% of the damaged lipid layer, DLL (partial volume fraction profiles in Fig. S9 of the SI). While the percentage of residual pristine bilayer is higher in this case compared to the previous sample, we have to remind that during the previous treatment the sample was exposed for a longer time (90 min × 3) to the $Cu(OH)_2/H_2O_2$ mixture compared to the current case, which could have also influenced the bilayer degradation.

Similar to the case presented above, a layer of water of about 15 Å is formed between solid substrate and SLB/DLL, a consequence of the formation of defects enhancing the bilayer permeability. In agreement with the higher film permeability, the water fraction in the LT layer of the residual SLB increases significantly, from 0 to 70%. The SLD for the DLL layer was again around zero, in agreement with the findings for the first SLB degradation.

As for the previous sample, we verified the reliability of our model to describe the post-peroxidation sample by comparing these results with the incoherent summation of reflectivities from the bilayer and bare SiO_2 surface (Fig. S10 and S11 of the SI). The fitting results for SLB/SiO_2 model (Fig. S10(D)–(F)) are compared to the fits for the pristine bilayer (Fig. S10(A)–(C)). The poorer fit quality of this scenario compared to the SLB/DLL model in Fig. 5D is clear in this case, with the traces of the best fitting model being unable to describe the oscillation at $q > 0.10$ Å, a signature of the thin DLL layer formed from the partial bilayer degradation. A schematic illustration summarizing the experimental study, including the bilayer formation, the nanoparticles injection and sedimentation, the production of ROS in presence of H_2O_2 and the results of the lipid peroxidation, *i.e.* a mixed sample of residual bilayer and degraded lipid layer, is reported in Fig. 6.

From the structural parameters obtained from the data analysis of the NR data (Tables S1 and S2 in the SI), it is possible to estimate the area per lipid, A_{lip}, from the following relation,

$$A_{lip} = \frac{V_{lip}}{D_{lip}} \quad (2)$$

where V_{lip} is the molecular volume of the phospholipid and D_{lip} is a parameter which describes the amount of phospholipid in a single bilayer unit, expressed in volume per surface area:[73]

$$D_{lip} = \int_{-\infty}^{+\infty} \phi_{lip}(z)\mathrm{d}z \quad (3)$$

Here, D_{lip} has the unit of a linear dimension, and it corresponds to the thickness of an equivalent layer composed entirely of the bilayer unit (lip = LH + LT + LH). This implies that it can be estimated from the measured bilayer thickness, d_{lip}, and the fraction of the lipid in the layer, $\phi_{lip} = 1 - \phi_w^{lip}$, where ϕ_w^{lip} is the volume fraction of water in the bilayer unit,

$$d_{lip} = \frac{D_{lip}}{\phi_{lip}} \quad (4)$$

For the pristine lipid bilayers used in our studies, this calculation gives an area per lipid $A_{lip}^{NR} = 60.7\ (\pm 0.9)$ Å^2, in excellent agreement with previous literature findings.[74] This result can be compared to the area per lipid calculated from the QCM-D data reported in Section 3.1. Under the validity of the Sauerbrey equation ($\Delta D/\Delta f \ll 1/f_0$, where f_0 is the fundamental resonance frequency of the quartz crystal), we can apply the well-known equation

$$\Delta m = -\frac{\sqrt{\mu_q \rho_q}}{2{f_{0,n}}^2}\frac{\Delta f_n}{n} \quad (5)$$

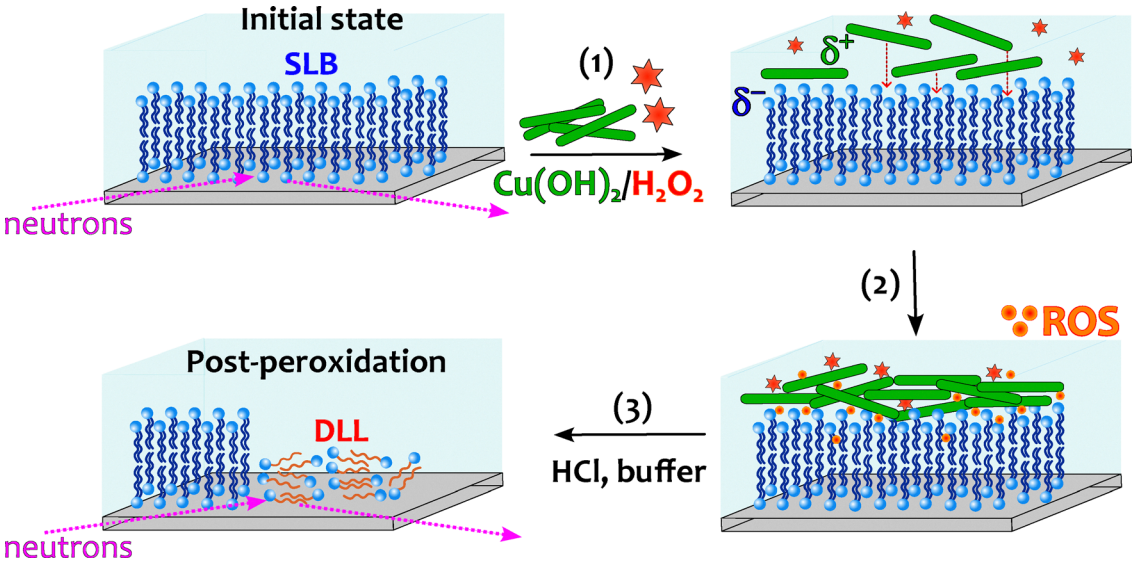

Fig. 6 Schematic representation of the lipid bilayer degradation induced by peroxidation. Initial state: dense supported lipid bilayer (SLB) onto the silicon substrate, characterized by full q-range NR. (1) Injection of $Cu(OH)_2$ nanoparticles in presence of millimolar concentration of oxygen peroxide. (2) The nanoparticles accumulate onto the lipid surface, where reactive oxygen species (ROS) are produced. These radicals diffuse inside the bilayer and provoke the breakage of the unsaturated alkyl chains. (3) Upon rinsing with acidic and buffer solution for the complete solubilization and removal of the nanoparticles, the residual sample is characterized by full q-range NR, revealing its transformation to mixed domains of residual bilayer and single degraded lipid layer (DLL).

where Δm is the areal sensed mass by the sensor, μ_q the shear elastic modulus of the quartz, ρ_q the quartz density, $f_{0,n}$ the resonant frequency and Δf_n the change of resonance frequency at the nth harmonic. From the areal sensed mass, we can estimated the corresponding number of molecules per unit area, and therefore their molecular area, $A_{lip}^{QCM\text{-}D}$ = 62.0 (± 0.5) Å^2, in excellent agreement with the result from NR data and previous literature.[74] This result is an additional proof of the high reproducibility of the bilayer structure by the method adopted in this study.

3.3.1 Kinetics of bilayer degradation at high peroxide concentration. For the second peroxidation experiment, the kinetic monitoring of the reflectivity during the nanorods incubation in presence of 30 mM H_2O_2 is reported in Fig. 7A. The color gradient from darker to lighter corresponds to increasing time, as well as the direction of the black arrow. The inset of this figure reports the variation of reflectivity Rq^4 extracted at q = 0.05 Å^{-1}, an arbitrary q-position but within the region of highest sensitivity to the variation of the LT hydration. The kinetics acquisition started very shortly after the H_2O_2 injection, and as highlighted in the inset of the figure the experimental data showed a clear decrease of the reflectivity within the first 10 min, with a stronger decrease compared to low H_2O_2 concentration (Fig. S7C).

Finally, to highlight the overall reflectivity variation between initial, intermediate (at the end of incubation, before rinsing) and final state (including the complete nanorods removal by HCl rinse), the reflectivity of each of these states in NPMW is compared in Fig. 7B. It is possible to identify a shift of the reflectivity minimum to higher q upon exposure to $Cu(OH)_2/H_2O_2$, a possible contribution of the DLL to the total reflectivity, and a sequential decrease of the reflected intensity from pristine SLB to degraded system, likely due to the removal of lipids from the substrate, which lose their tight assembly upon peroxidation.[75] Although the kinetic monitoring in Fig. 7A did not provide a continuous decrease in Rq^4 over time as a signature of the ongoing lipid peroxidation, the comparison of the full q-range reflectivities of the three characteristic states in Fig. 7B demonstrates the structural variation of the lipidic film due to peroxidation.

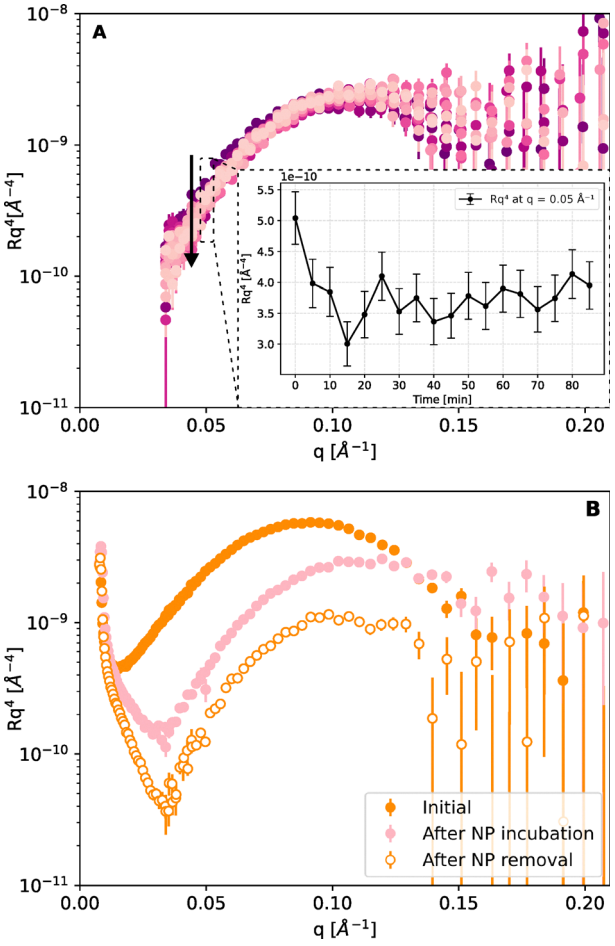

Fig. 7 (A) Variation of the reflectivity profile in the mid-q range for a POPE:POPG bilayer in contact with $Cu(OH)_2$ nanorods in presence of 30 mM H_2O_2. Each dataset corresponds to a 5-min acquisition for a total monitoring time of 90 min. The time increases from the darkest to the lightest curve, as indicated by the arrow. The inset of the image reports the variation of Rq^{-4} as a function of time at q = 0.05 Å^{-1}. (B) Reflectivity data in NPMW for pristine bilayer (Initial), after incubation with $Cu(OH)_2$ nanoparticles (90 min), and after rinsing with 1 M HCl solution for NP removal).

3.4 Control experiment

As a control sample, a third lipid bilayer with the same lipid composition was studied by NR before and after exposure to increasing peroxide concentration, 0.1 mM and 30 mM H_2O_2, and 1 M HCl rinse, but without any exposure to the $Cu(OH)_2$ nanorods. The reflectivity data and best fitting curves, along with the SLD and volume fraction distribution, are reported in Fig. S11 of the SI. The corresponding best fitting parameters are listed in Table S3. The results demonstrate the absence of the bilayer degradation in absence of $Cu(OH)_2$, and therefore they prove their essential role to produce the oxygen radicals responsible of the lipid peroxidation.

4 Conclusions

This work presents the degradation of a (POPE:POPG) lipid bilayer modeling the membrane of *E. coli* in contact to copper hydroxide ($Cu(OH)_2$) nanorods in the presence of millimolar concentrations of H_2O_2 in water. QCM-D and neutron reflectometry (NR) were used to monitor the structural changes of the phospholipid bilayer exposed to the oxidative environment. The preparation of model *E. coli* phospholipid membranes onto a large silicon substrate, suitable for neutron reflectometry (NR) experiments, was an experimental challenge of this study. The preparation protocol based on the SALB method allowed to overcome the technical constraints inherent in the vesicle fusion method for this specific lipid mixture, such as high temperature, small size and monodispersity, osmotic shock and ionic environment to prevent vesicles aggregation. The high quality of the supported POPE:POPG lipid bilayer was clearly demonstrated by NR experiments using three different isotopic contrasts. Thanks to its simplicity and versatility, the SALB method offers the possibility of preparing biomimetic membranes from a mixture of highly charged lipids, weakly

charged substrates or lipids with a non-conical shape, thus opening the way to new studies in the field of biomimetic interfaces. Our previous EPR study had shown that copper hydroxide nanorods were able to dissociate hydrogen peroxide into hydroxyl radicals without releasing into water cupric ions. Now, when a suspension of $Cu(OH)_2$ nanorods was injected on the top of this bilayer in the presence of H_2O_2, QCM-D and NR provide evidence that these particles deposit on the bilayer, and they peroxidize the phospholipids by the hydroxyl radicals produced in the oxidative environment. The analyses of NR data reveal that this peroxidation left a macroscopically heterogeneous film on the silicon substrate, with the coexistence of the residual pristine supported lipid bilayer (SLB) and a degraded lipid layer (DLL). Successive exposure to H_2O_2 concentrations of 0.1, 0.3 and then 30 mM for 90 minutes each (total exposure time of 270 minutes) produced greater degradation of the bilayer than a single 90-minute exposure to the maximum H_2O_2 concentration of 30 mM. This result suggests that prolonged exposure to small quantities of radicals (low H_2O_2 concentration) is more effective in peroxidizing the phospholipids, as at high H_2O_2 concentration the radicals recombine before reacting with the lipids in the bilayer. Finally, this neutron reflectometry study shows that the peroxidation of phospholipids breaks their bilayer arrangement, and the consequent increase of membrane permeability could be the key phenomenon leading ultimately to the death of Gram-negative bacteria, such as *E. coli* by membrane lysis.

Due to their extremely low solubility at neutral pH (limiting the release of cupric ions) and a high bactericidal activity, $Cu(OH)_2$ nanorods could be added to the filter medium of an irrigation water disinfection system in agriculture or deposited onto surface in hospitals with a potential self-disinfecting activity. Our simple but accurate methodology to study the effect of lipid peroxidation by copper containing nanoparticles will be further extended to more complex biomimetic systems, considering the inclusion of cardiolipin in the model system, a lipid contributing to the stability of intracellular cytoplasmic membrane in *E. coli*.[76,77] Surface imaging techniques (*e.g.*, AFM or cryo-SEM) could be also implemented to characterize also the surface morphology and the lateral extension of each domain, and validate the structural characterization performed by these QCM-D and NR studies. The established methodology can be extended to the study of different nanoparticle chemistry and various biomimetic membranes, giving the opportunity to support the design of antibacterial formulations by fundamental research.

Author contributions

SM: conceptualization, data curation, formal analysis, funding acquisition, investigation, software, writing – original draft, writing – review & editing. HR: data curation, formal analysis, software. NP: investigation, software. GC: conceptualization, funding acquisition, investigation, resources, writing – original draft, writing – review & editing.

Conflicts of interest

The authors have no conflicts to declare.

Data availability

As stated in the main text of the manuscript, the data reported in this article are available at DOI: **https://doi.org/10.5291/ILL-DATA.9-13-1132.** The script for the data analysis used with the software *refnx* is available from the public repository Zenodo at DOI: **https://doi.org/10.5281/zenodo.15691332**.

Supplementary information (SI) is available. See DOI: **https://doi.org/10.1039/d5sm00809c**.

Acknowledgements

SM and GC acknowledge the Institut Laue-Langevin (ILL) for the allocation of beamtime (doi: **https://doi.org/10.5291/ILL-DATA.9-13-1132**), and the Partnership for Soft Condensed Matter (PSCM) to grant access to the support laboratories for all preliminary studies and the sample preparation for beamtime. SM and GC also would like to thank the Research Group (GdR 3751) 'Bio-engineering of interfaces (B2i)' funded by the CNRS (France), and its coordinators, V. Humblot, L. Vellutini and Y. Roupioz, for creating the opportunity for this research study to come about. HR gratefully acknowledges the Career Bridging Grant of the Technische Universität Darmstadt.

Notes and references

1 WHO and EDC, *Antimicrobial resistance surveillance in Europe, 2023–2021 data*, 2023.

2 A. Cassini, L. D. Högberg, D. Plachouras, A. Quattrocchi, A. Hoxha, G. S. Simonsen, M. Colomb-Cotinat, M. E. Kretzschmar, B. Devleesschauwer, M. Cecchini, D. A. Ouakrim, T. C. Oliveira, M. J. Struelens, C. Suetens, D. L. Monnet, R. Strauss, K. Mertens, T. Struyf, B. Catry, K. Latour, I. N. Ivanov, E. G. Dobreva, A. T. Andraševic, S. Soprek, A. Budimir, N. Paphitou, H. Žemlicková, S. S. Olsen, U. W. Sönksen, P. Märtin, M. Ivanova, O. Lyytikäinen, J. Jalava, B. Coignard, T. Eckmanns, M. A. Sin, S. Haller, G. L. Daikos, A. Gikas, S. Tsiodras, F. Kontopidou, Á. Tóth, Á. Hajdu, Ó. Guólaugsson, K. G. Kristinsson, S. Murchan, K. Burns, P. Pezzotti, C. Gagliotti, U. Dumpis, A. Liuimiene, M. Perrin, M. A. Borg, S. C. de Greeff, J. C. Monen, M. B. Koek, P. Elstrøm, D. Zabicka, A. Deptula, W. Hryniewicz, M. Caniça, P. J. Nogueira, P. A. Fernandes, V. Manageiro, G. A. Popescu, R. I. Serban, E. Schréterová, S. Litvová, M. Štefkovicová, J. Kolman, I. Klavs, A. Korošec, B. Aracil, A. Asensio, M. Pérez-Vázquez, H. Billström, S. Larsson, J. S. Reilly, A. Johnson and S. Hopkins, *Lancet Infect. Dis.*, 2019, **19**, 56–66.

3 C. Daniau, A. Paumier, H. Blanchard, B. Nkoumazok, M. Angibaud, M. Chartier, A. Savey, A. Machut, M. Pefau, J.-C. Delaroziere, E. Porier, C. Mourlan, S. Alfandari, O. Bajolet, C. Lawrence, Y. L. Strat, A. Berger-Carbane, D. Che and B. Coignard, *Principaux résultats de l'enquête nationale de*

prévalence 2022 des infections nosocomiales et des traitements anti-infectieux en établissements de santé, Santé publique france technical report, 2023.
4 A. Catalano, D. Iacopetta, J. Ceramella, D. Scumaci, F. Giuzio, C. Saturnino, S. Aquaro, C. Rosano and M. S. Sinicropi, *Molecules*, 2022, **27**, 1–18.
5 K. W. K. Tang, B. C. Millar and J. E. Moore, *Br. J. Biomed. Sci.*, 2023, **80**, 1–11.
6 Z. Breijyeh, B. Jubeh and R. Karaman, *Molecules*, 2020, **25**, 1–23.
7 S. K. Ahmed, S. Hussein, K. Qurbani, R. H. Ibrahim, A. Fareeq, K. A. Mahmood and M. G. Mohamed, *J. Med., Surgery, Public Health*, 2024, **2**, 1–9.
8 M. Naghavi, *et al.*, *The Lancet*, 2024, **404**, 1199–1226.
9 L. Caselli, E. Parra-Ortiz, S. Micciulla, M. W. Skoda, S. M. Häffner, E. M. Nielsen, M. J. van der Plas and M. Malmsten, *Small*, 2024, **20**, 1–16.
10 L. Caselli, G. Du, S. Micciulla, T. Traini, F. Sebastiani, R. G. Diedrichsen, S. Köhler, M. W. Skoda, M. J. van der Plas and M. Malmsten, *ACS Appl. Mater. Interfaces*, 2024, 60056–60069.
11 M. M. Gaschler and B. R. Stockwell, *Biochem. Biophys. Res. Commun.*, 2017, **482**, 419–425.
12 L. J. Su, J. H. Zhang, H. Gomez, R. Murugan, X. Hong, D. Xu, F. Jiang and Z. Y. Peng, *Oxid. Med. Cell. Longevity*, 2019, **2019**, 1–13.
13 H. T. Endale, W. Tesfaye and T. A. Mengstie, *Front. Cell Dev. Biol.*, 2023, **11**, 1–7.
14 B. Halliwell, *Am. J. Med.*, 1991, **91**, S14–S22.
15 H. Cao, S. F. Xiong, L. L. Dong and Z. T. Dai, *Molecules*, 2024, **29**, 1–16.
16 E. Sanchez-Lopez, D. Gomes, G. Esteruelas, L. Bonilla, A. L. Lopez-Machado, R. Galindo, A. Cano, M. Espina, M. Ettcheto, A. Camins, A. M. Silva, A. Durazzo, A. Santini, M. L. Garcia and E. B. Souto, *Nanomaterials*, 2020, **10**, 1–39.
17 M. Paschoalino, N. C. Guedes, W. Jardim, E. Mielczarski, J. A. Mielczarski, P. Bowen and J. Kiwi, *J. Photochem. Photobiol., A*, 2008, **199**, 105–111.
18 C. Gunawan, W. Y. Teoh, C. P. Marquis and R. Amal, *ACS Nano*, 2011, **5**, 7214–7225.
19 G. Applerot, J. Lellouche, A. Lipovsky, Y. Nitzan, R. Lubart, A. Gedanken and E. Banin, *Small*, 2012, **8**, 3326–3337.
20 A. Azam, A. S. Ahmed, M. Oves, M. S. Khan and A. Memic, *Int. J. Nanomed.*, 2012, **7**, 3527–3535.
21 C. Angelé-Martínez, K. V. T. Nguyen, F. S. Ameer, J. N. Anker and J. L. Brumaghim, *Nanotoxicology*, 2017, **11**(2), 278–288.
22 B. Clavier, A. Zhadan, T. Baptiste, F. Boucher, A. Guiet, F. Porcher, V. Brezová, C. Roques and G. Corbel, *Dalton Trans.*, 2022, **51**, 8411–8424.
23 B. Clavier, T. Baptiste, A. Zhadan, A. Guiet, F. Boucher, V. Brezová, C. Roques and G. Corbel, *J. Mater. Chem. B*, 2022, **10**, 779–794.
24 W. Dröge, *Physiol. Rev.*, 2002, **82**, 47–95.
25 C. D. Pericone, K. Overweg, P. W. M. Hermans and J. N. Weiser, *Infect. Immun.*, 2000, **68**, 3990–3997.
26 A. N. Pham, G. Xing, C. J. Miller and T. D. Waite, *J. Catal.*, 2013, **301**, 54–64.
27 Z.-H. Zhao, Y. Sakagami and T. Osaka, *Bull. Chem. Soc. Jpn.*, 2006, **71**, 939–945.
28 J. O. Noyce, H. Michels and C. W. Keevil, *J. Hosp. Infect.*, 2006, **63**, 289–297.
29 S. W. J. Gould, M. D. Fielder, A. F. Kelly, M. Morgan, J. Kenny and D. P. Naughton, *Ann. Microbiol.*, 2009, **59**, 151–156.
30 I. Platzman, R. Brener, H. Haick and R. Tannenbaum, *J. Phys. Chem. C*, 2008, **112**, 1101–1108.
31 J. C. Henderson, S. M. Zimmerman, A. A. Crofts, J. M. Boll, L. G. Kuhns, C. M. Herrera and M. S. Trent, *Annu. Rev. Microbiol.*, 2016, **70**, 255–278.
32 N. Shaw, in *Advances in Applied Microbiology*, ed. D. Perlman, Academic Press, 1974, vol. 17, pp. 63–108.
33 E. J. J. Lugtenberg and R. Peters, *Biochim. Biophys. Acta*, 1976, **441**(1), 38–47.
34 M. Bogdanov, K. Pyrshev, S. Yesylevskyy, S. Ryabichko, V. Boiko, P. Ivanchenko, R. Kiyamova, Z. Guan, C. Ramseyer and W. Dowhan, *Sci. Adv.*, 2020, 1–13.
35 L. K. Tamm and H. M. McConnell, *Biophys. J.*, 1985, **47**, 105–113.
36 R. P. Richter, R. Bérat and A. R. Brisson, *Langmuir*, 2006, **22**, 3497–3505.
37 E. T. Castellana and P. S. Cremer, *Surf. Sci. Rep.*, 2006, **61**, 429–444.
38 J. Kurniawan, J. F. V. D. Souza, A. T. Dang, G. Y. Liu and T. L. Kuhl, *Langmuir*, 2018, **34**, 15622–15639.
39 S. Helmy, P. Brocca, A. Koutsioubas, S. C. Hall, L. Puricelli, P. Parisse, L. Casalis and V. Rondelli, *J. Colloid Interface Sci.*, 2025, **690**, 1–14.
40 M. E. Villanueva, L. Bar, L. Porcar, Y. Gerelli and P. Losada-Pérez, *J. Colloid Interface Sci.*, 2025, **677**, 620–631.
41 B. Lu, T. Smith and J. J. Schmidt, *Nanoscale*, 2015, **7**, 7858–7866.
42 J. A. Zasadzinski, R. Viswanathan, L. Madsen, J. Garnaes and D. K. Schwartz, *Science*, 1994, **263**, 1726–1733.
43 T. K. Lind and M. Cárdenas, *Biointerphases*, 2016, **11**, 1–12.
44 Z. V. Leonenko, A. Carnini and D. T. Cramb, *Biochim. Biophys. Acta, Biomembr.*, 2000, **1509**, 131–147.
45 K. Morigaki and K. Tawa, *Biophys. J.*, 2006, **91**, 1380–1387.
46 A. Luchini and G. Vitiello, *Biomimetics*, 2021, **6**, 1–18.
47 A. H. Beaven, C. Arnarez, E. Lyman, W. F. Bennett and A. J. Sodt, *J. Phys. Chem. B*, 2021, **125**, 1815–1824.
48 J. A. Jackman and N. J. Cho, *Langmuir*, 2020, **36**, 1387–1400.
49 J. A. Jackman, M. C. Kim, V. P. Zhdanov and N. J. Cho, *Phys. Chem. Chem. Phys.*, 2016, **18**, 3065–3072.
50 M. E. Villanueva, L. Bar and P. Losada-Pérez, *Colloids Surf., A*, 2024, **682**, 1–12.
51 E. Reimhult, F. Höök and B. Kasemo, *Langmuir*, 2003, **19**, 1681–1691.
52 E. Oh, J. A. Jackman, S. Yorulmaz, V. P. Zhdanov, H. Lee and N. J. Cho, *Langmuir*, 2015, **31**, 771–781.
53 M. Dacic, J. A. Jackman, S. Yorulmaz, V. P. Zhdanov, B. Kasemo and N. J. Cho, *Langmuir*, 2016, **32**, 6486–6495.
54 T. K. Lind, M. W. Skoda and M. Cárdenas, *ACS Omega*, 2019, **4**, 10687–10694.
55 A. R. Ferhan, B. K. Yoon, S. Park, T. N. Sut, H. Chin, J. H. Park, J. A. Jackman and N. J. Cho, *Nat. Protoc.*, 2019, **14**, 2091–2118.

56 G. Cordoyiannis, L. Bar, M. E. Villanueva, S. Neupane and P. Losada-Pérez, in *Advances in Biomembranes and Lipid Self-Assembly*, ed. A. Iglic, M. Rappolt and P. Losada Perez, Academic Press, 2023, vol. 37 of Advances in Biomembranes and Lipid Self-Assembly, pp. 61–88.
57 J. J. Gillissen, S. R. Tabaei and N. J. Cho, *Phys. Chem. Chem. Phys.*, 2016, **18**, 24157–24163.
58 R. Augustine and A. Hasan, *J. Drug Delivery Sci. Technol.*, 2020, **56**, 1–12.
59 H. D. Lutz, H. Müller and M. Schmidt, *J. Mol. Struct.*, 1994, **328**, 121–132.
60 P. Kienzle, *Neutron activation and scattering calculator*, **https://www.ncnr.nist.gov/resources/activation/**.
61 DOI: **10.5291/ILL-DATA.9-13-1132**.
62 R. A. Campbell, H. P. Wacklin, I. Sutton, R. Cubitt and G. Fragneto, *Eur. Phys. J. Plus*, 2011, **126**, 1–22.
63 A. R. Nelson and S. W. Prescott, *J. Appl. Crystallogr.*, 2019, **52**, 193–200.
64 , DOI: **10.5281/zenodo.15691332**.
65 K. A. Runas and N. Malmstadt, *Soft Matter*, 2015, **11**, 499–505.
66 D. Johannsmann, *Phys. Chem. Chem. Phys.*, 2008, **10**, 4516–4534.
67 J. A. Jackman, J. H. Choi, V. P. Zhdanov and N. J. Cho, *Langmuir*, 2013, **29**, 11375–11384.
68 B. Gonzalez-Flechat and B. Demple, *J. Biol. Chem.*, 1995, **270**, 13681–13687.
69 A. Rodríguez-Rojas, J. J. Kim, P. R. Johnston, O. Makarova, M. Eravci, C. Weise, R. Hengge and J. Rolff, *PLoS Genet.*, 2020, **16**, 1–33.
70 C. M. Reynolds, O. C. Fiebig, A. Marroquin, A. J. Glaid, K. Chokhany, R. G. Zdenek, M. L. da Cruz Garcia and P. S. Cremer, *J. Am. Chem. Soc.*, 2025, **147**, 8386–8397.
71 J. A. Imlay and S. Linn, *J. Bacteriol.*, 1986, **166**, 519–527.
72 J. A. Imlay, S. M. Chin and S. Linn, *Science*, 1988, **240**, 640–642.
73 S. Micciulla, Y. Gerelli and E. Schneck, *Biophys. J.*, 2019, **116**, 1259–1269.
74 K. Murzyn, T. Róg and M. Pasenkiewicz-Gierula, *Biophys. J.*, 2005, **88**, 1091–1103.
75 J. Wong-Ekkabut, Z. Xu, W. Triampo, I. M. Tang, D. P. Tieleman and L. Monticelli, *Biophys. J.*, 2007, **93**, 4225–4236.
76 W. S. Yeo, S. Dyzenhaus, V. J. Torres, S. R. Brinsmade and T. Bae, *Infect. Immun.*, 2023, **91**, 1–12.
77 V. A. M. Gold, A. Robson, H. Bao, T. Romantsov, F. Duong and I. Collinson, *Proc. Natl. Acad. Sci. U. S. A.*, 2010, **107**, 10044–10049.

